

Supplementary Information

PBTTT-C₁₆ sol-gel transition by rod associations and networking

Han-Liou Yi and Chi-Chung Hua*

Department of Chemical Engineering, National Chung Cheng University, Chiayi 62102, Taiwan

S1 Absorbance of Lw-pBTTT-C₁₆/CB sol and gel

A UV-vis spectrometer (JASCO, V-570) was employed to examine the absorbance of Lw-pBTTT-C₁₆/CB sol and gel. The measurement was conducted with a cell having a path length of 2 mm (Hellma, 110-QS) to minimize the scattering associated with large pBTTT-C₁₆ clusters. Fig. S1a reveals that the present Lw-pBTTT-C₁₆/CB sample has negligible absorption at the incident light wavelength ($\lambda_0 = 785$ nm) in this study.

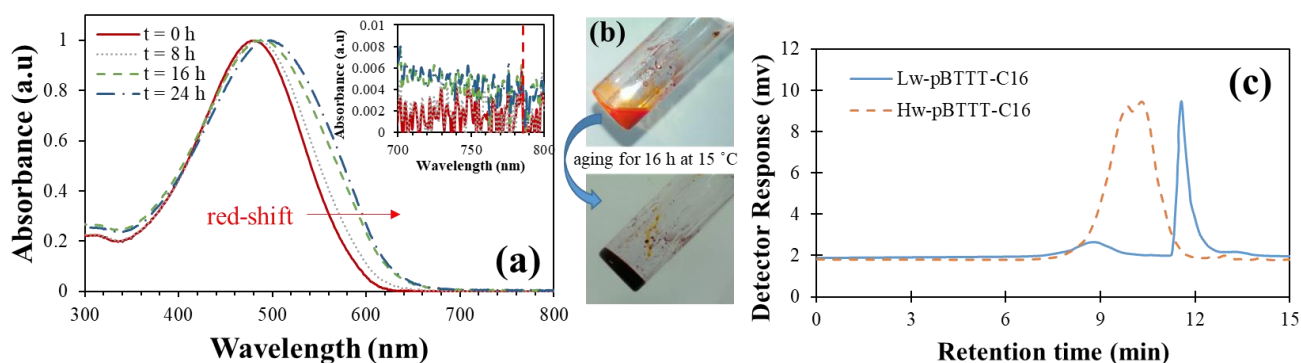


Fig. S1 (a) Time evolutions of the UV-vis absorption spectra during the Lw-pBTTT-C₁₆/CB sol-gel transition at $T = 15$ °C, wherein results at four different gelation times are shown: $t = 0$ h (solid line), 8 h (dotted line), 16 h (dashed line), and 24 h (dashed-dotted line). The absorption at 785 nm is marked by the vertical dashed line in the magnified inset figure. (b) Photographs showing the appearance of the freshly prepared 10 mg mL⁻¹ Lw-pBTTT-C₁₆/CB solution and that of the corresponding gel after aging for 16 h at 15 °C. (c) Comparison of the original GPC data on the Lw-pBTTT-C₁₆ and Hw-pBTTT-C₁₆ samples in this study.

S2 Effect of laser power on the dynamics of the Lw-pBTTT-C₁₆/CB gel

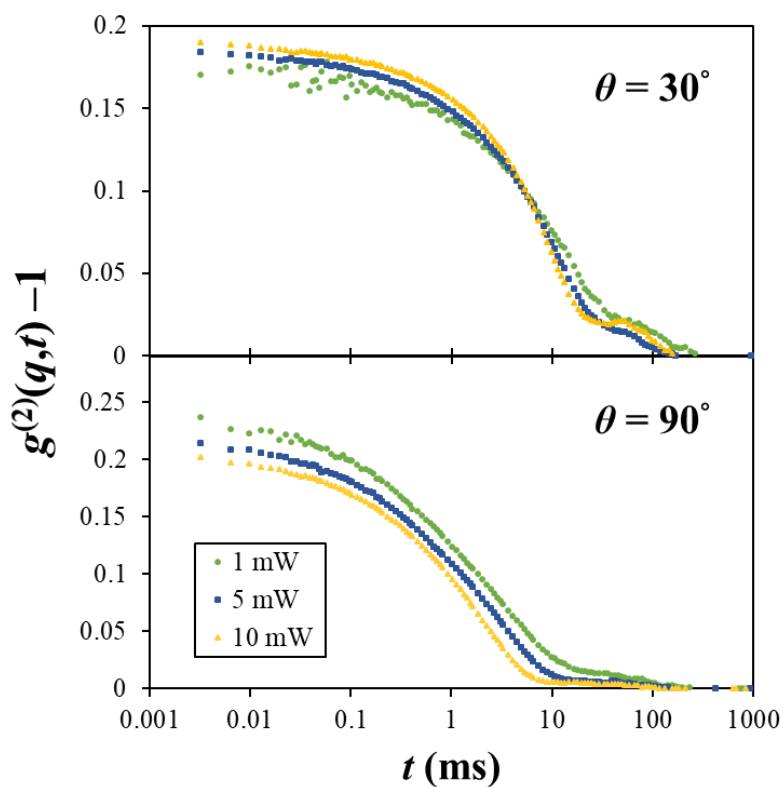


Fig. S2 Intensity correlation functions, $g^{(2)}(q,t) - 1$, for the Lw-pBTTT-C₁₆/CB gel incubated at $T = 15$ °C ($t = 24$ h), with the laser power equal to 5, 10 or 50% of the original intensity (*i.e.*, 20 mW). Given that the results differ only slightly for the incident laser powers investigated, the one with 5% of its original intensity (1 mW) was used in this study.

S3 Assessment of ergodicity of Lw-pBTTT-C₁₆/CB gel

As detailed in prior work,¹ the effects of ergodicity for the Lw-pBTTT-C₁₆/CB solution and gel may be investigated using the results shown in Fig. S3-S5. The results bear similar features as commonly observed for gelation samples. In particular, the disparity between the ensemble-averaged scattering intensity, $\langle I \rangle_E$, and the dynamic mobile component, $\langle I_d \rangle_T$, extracted in Fig. S4 from the time-averaged scattering intensity, $\langle I \rangle_T$, reflects the degree of nonergodicity for the Lw-pBTTT-C₁₆/CB samples investigated. It should also be clear from the results shown in Fig. S5 that the intensity correlation functions $g^{(2)}(q,t) - 1$ for different sample positions differ only in the initial intensity and the relaxation behavior is similar in all cases.

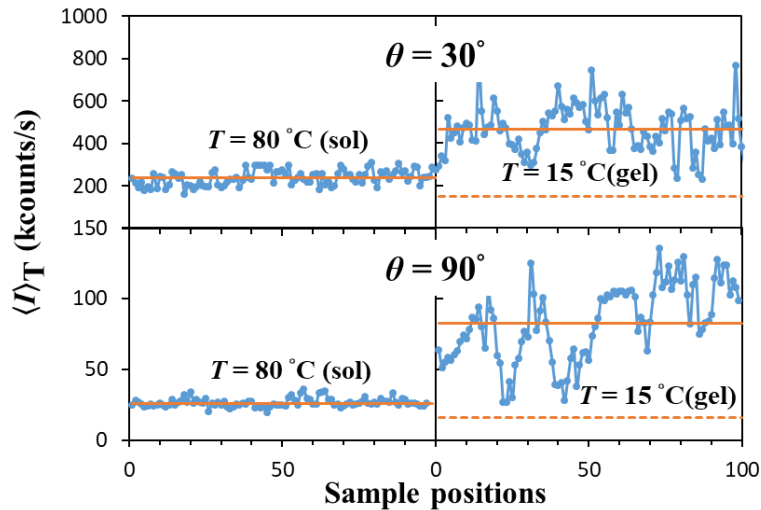


Fig. S3 Sample-position dependences of the time-averaged scattering intensity, $\langle I \rangle_T$, for the Lw-pBTTT-C₁₆/CB solution ($T = 80^\circ\text{C}$) and gel ($T = 15^\circ\text{C}$; $t = 24\text{ h}$) at two representative scattering angles $\theta = 30^\circ$ and 90° . The horizontal dashed and solid lines represent the results for $\langle I_d \rangle_T$ and $\langle I \rangle_E$, respectively.

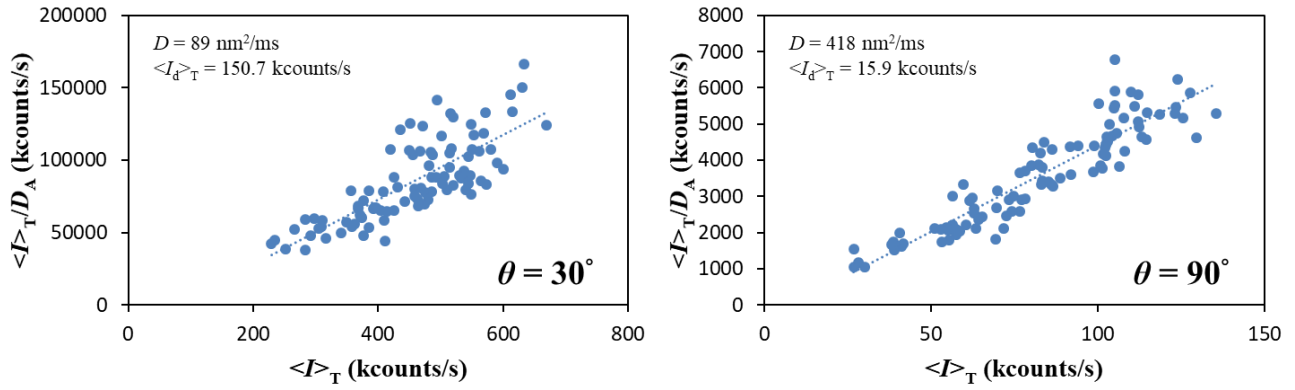


Fig. S4 Plots of $\langle I \rangle_T / D_A$ versus time-averaged scattering intensity, $\langle I \rangle_T$, for the Lw-pBTTT-C₁₆/CB gel incubated at 15 °C ($t = 24$ h), wherein the collective diffusion coefficient, D , and the dynamic mobile component, $\langle I_d \rangle_T$, are obtained simultaneously by the slope and intercept, respectively.

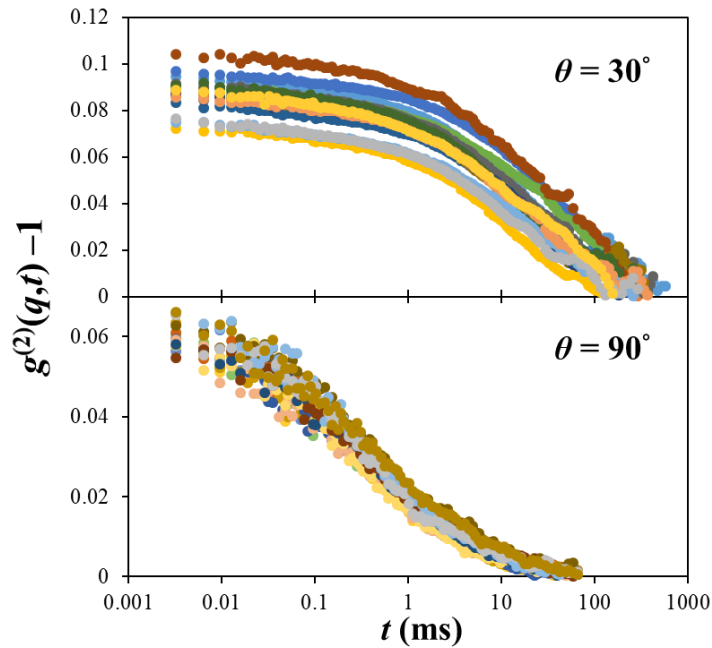


Fig. S5 Intensity correlation functions, $g^{(2)}(q, t) - 1$, measured at two representative scattering angles $\theta = 30^\circ$ and 90° for different sample positions as considered in Fig. S3 for the Lw-pBTTT-C₁₆/CB gel incubated at 15 °C ($t = 24$ h).

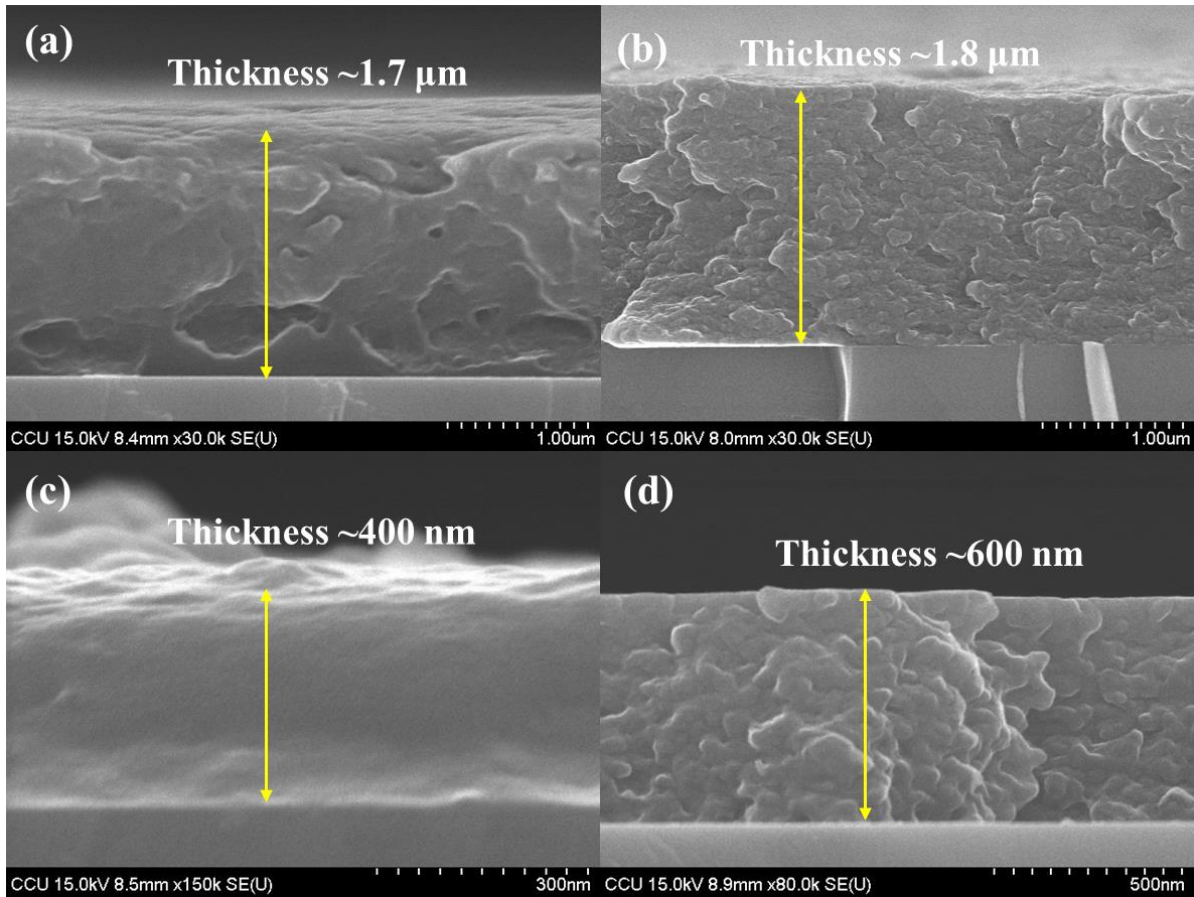


Fig. S6 Cross-sectional SEM images of (a) Lw-pBTTT-C₁₆ gel, (b) Hw-pBTTT-C₁₆ gel, (c) Lw-pBTTT-C₁₆ drop-cast thin film, and (d) Hw-pBTTT-C₁₆ drop-cast thin film.

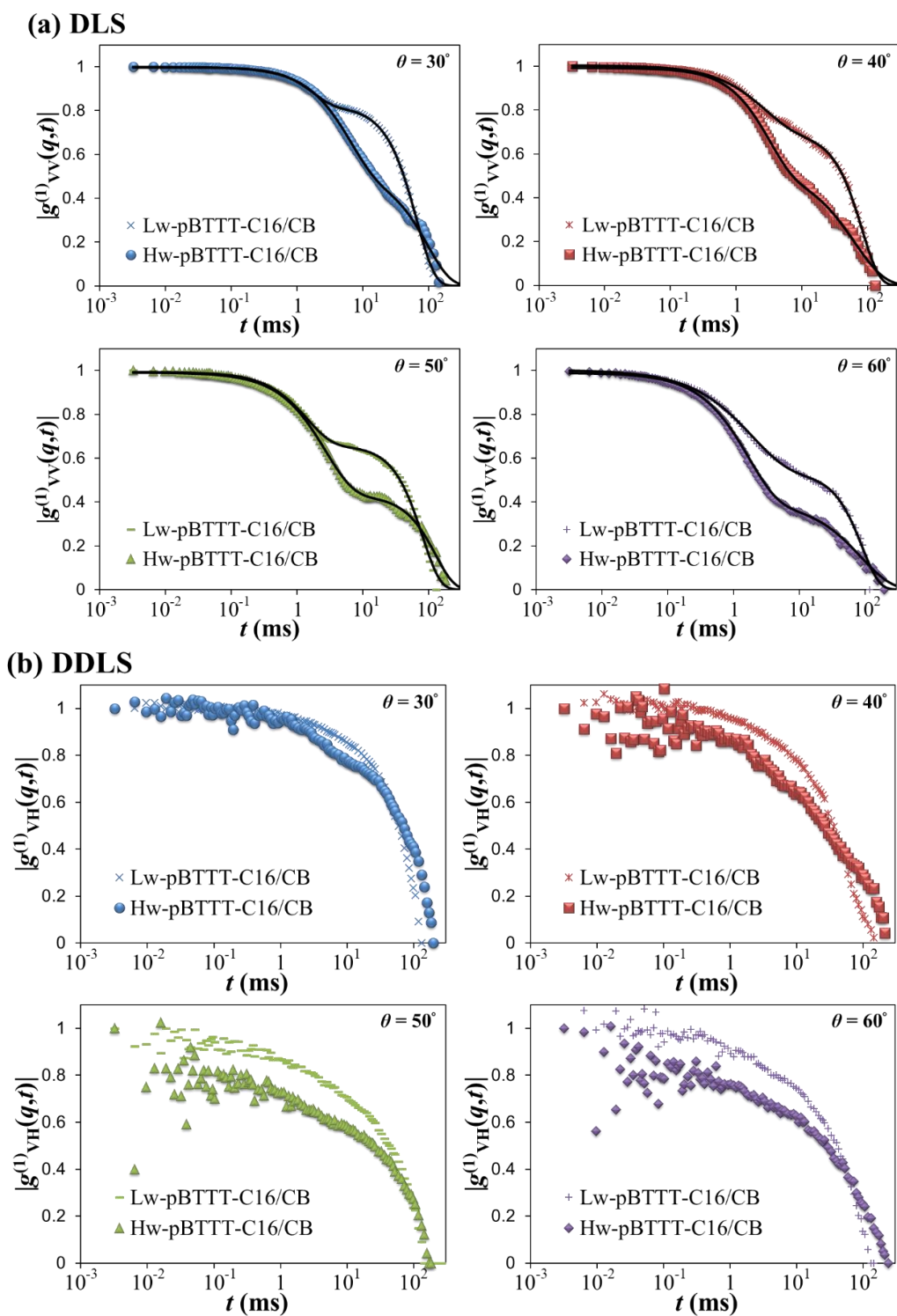


Fig. S7 Field autocorrelation functions, $|g^{(1)}(q,t)|$, in (a) DLS and (b) DDLS experiments for the 10 mg mL⁻¹ Hw-pBTTT-C₁₆/CB and Lw-pBTTT-C₁₆/CB solutions at $T = 80$ °C. The solid lines (for DLS data) represent the results of nonlinear least-square fits using eqn (S2) in prior work;¹ see fitted material properties gathered in Table S1.

Table S1 Parameter values extracted from full-curve fits of the DLS data on two different pBTTT-C₁₆/CB

solutions at 80 °C

Parameters	Lw-pBTTT-C₁₆	Hw-pBTTT-C₁₆
Fraction of the collective diffusion mode (A)	0.32±0.12	0.53±0.06
Stretched exponent (α)	1.08±0.28	1.07±0.09
Collective diffusion coefficient ($D_{T, \text{fast}}$) [nm ² ·ms ⁻¹]		
- Length (L) [nm]	317±107	392±9
- Diameter (d) [nm]	156±100	201±45
- Aspect ratio	2.0	2.0
Stretched exponent (β)	1.64±0.05	1.17±0.28

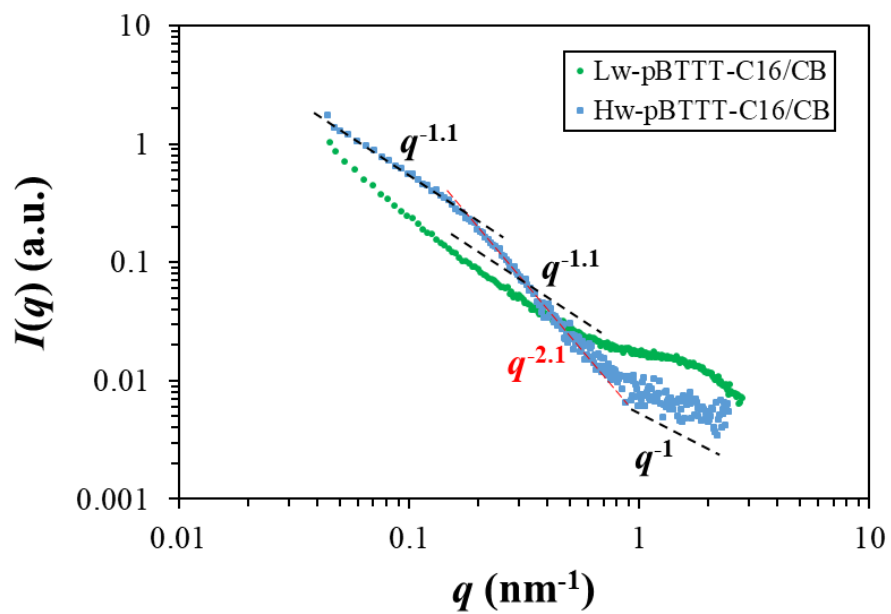


Fig. S8 SAXS profiles for the 10 mg mL^{-1} Hw-pBTTT-C₁₆/CB and Lw-pBTTT-C₁₆/CB solutions at $T = 80 \text{ }^\circ\text{C}$.

S4 Time-evolving DLS features during Lw-pBTTT-C₁₆/CB sol-gel transition

The DDLS profiles in Fig. S9b indicate that the Lw-pBTTT-C₁₆/CB sol ($t = 0$ h) begins with notably anisotropic aggregate state, whereas the Hw-pBTTT-C₁₆/CB sol consists of spherical aggregates without exhibiting discernible DDLS relaxation pattern.¹ Fig. S9a shows the time evolution of the normalized field autocorrelation function, $|g_{VV}^{(1)}(q,t)|$, for the Lw-pBTTT-C₁₆/CB gelation at 15 °C. The DLS relaxation evolves from the stretched-exponential behavior (up to $t = 8$ h) to power-law one, as often reported with polymer and colloid gelation.²⁻⁵ At $t = 0$ h, three DLS relaxation modes can be identified and analyzed in Fig. S10. Using the second relaxation mode as an example, the mean decay rate, $\langle \Gamma \rangle$, extracted from CONTIN is plotted as a function of q^2 and shown in the inset of Fig. S9b, confirming the diffusive attribute $\langle \Gamma_{VV} \rangle = D_T q^2$. The corresponding VH decay rate, $\langle \Gamma_{VH} \rangle$, shown in the same plot exhibits approximately the same slope and confirms the general relationship $\langle \Gamma_{VH} \rangle = D_T q^2 + 6D_R$ (D_T and D_R being the translational and rotational diffusivities, respectively.) The diffusion coefficients, along with the full-curve fitting, can be utilized to unambiguously determine the length L and diameter d of an anisotropic aggregate species within light scattering experiments, as we elucidated in prior work.⁶ Accordingly, the results shown in Table S2 indicate that the first and second relaxation modes represent isolated rodlike gelator ($L \sim 15.8$ nm and $d \sim 4.5$ nm) and cylindrical aggregates ($L \sim 160$ nm and $d \sim 30$ nm), respectively. The appearance of a plateau in $|g_{VV}^{(1)}(q,t)|$ at $t \sim 1$ ms and onward marks the existence of a third (slow) relaxation mode. Judged by its $\langle \Gamma \rangle \sim q^{0-1}$ dependence in Fig. S10 and, in particular, by the SALS feature discussed in the main text, this mode likely represents dynamically arrested microgels formed by cylindrical aggregates. With increased gelation time, the DLS features can

be captured quite well by using the formulations described in prior work.¹

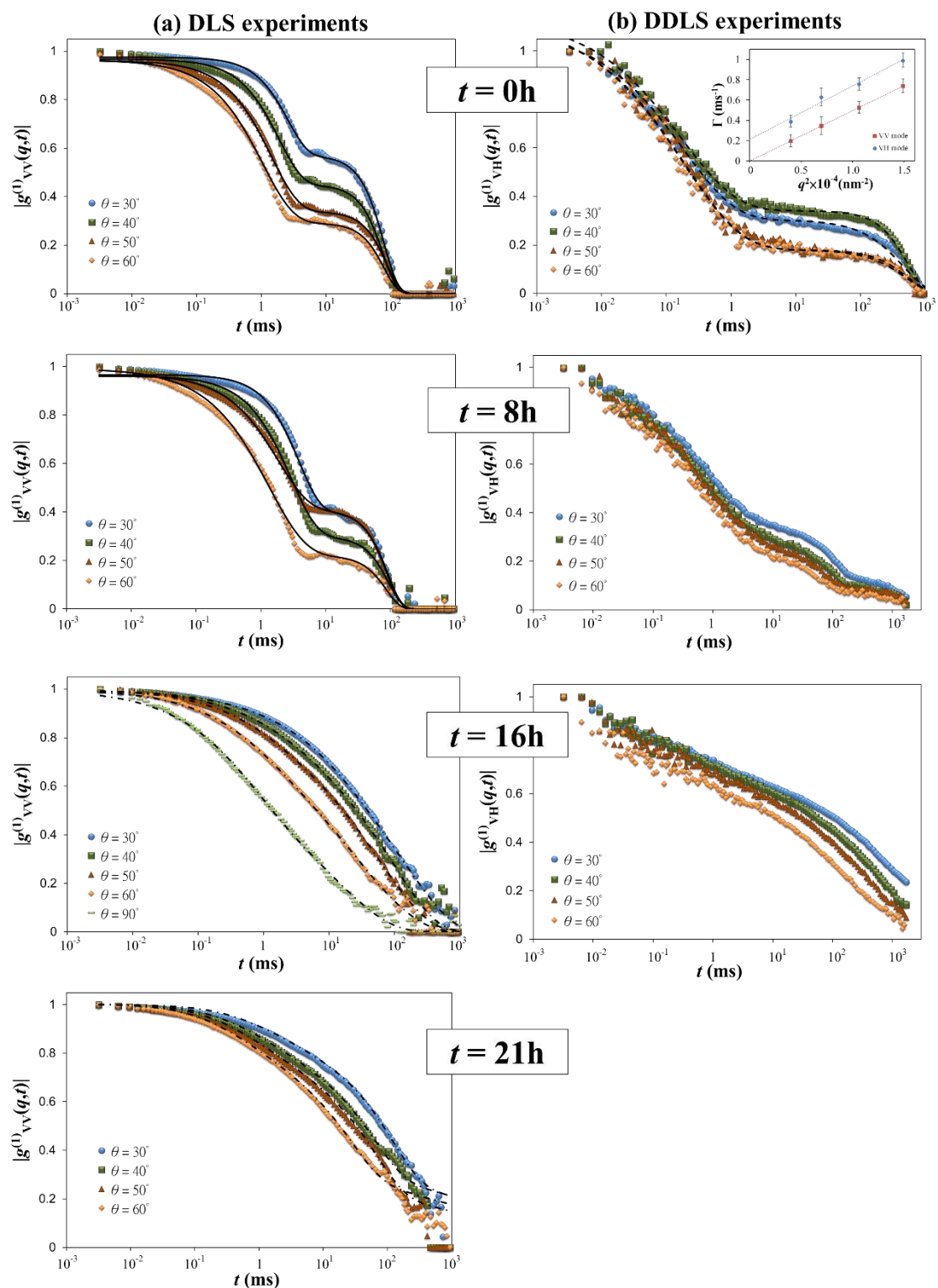


Fig. S9 Angular dependences of the field autocorrelation function, $|g^{(1)}(q, t)|$, in (a) DLS and (b) DDLS experiments with the 10 mg mL^{-1} Lw-pBTTT-C₁₆/CB gel fostered at $T = 15 \text{ }^\circ\text{C}$ as a function of the

gelation time. The inset figure in (b) sketches the mean decay rate, $\langle \Gamma \rangle$, as a function of q^2 from both experiments on the second relaxation mode. The solid and dashed lines for the initial sol state ($t = 0$ h) represent the results of full-curve (nonlinear least-square) fits with eqn (S2) (solid line; DLS data) and eqn (S3) (dashed line; DDLS data), respectively, described in prior work;¹ the DLS data for $t = 16$ and 21 h are fitted using eqn (S4) (dashed-dotted lines). Some of the parameter values extracted in the model fits are selectively listed in Table S2, and the physical significance associated with each term may be found in the same reference article.

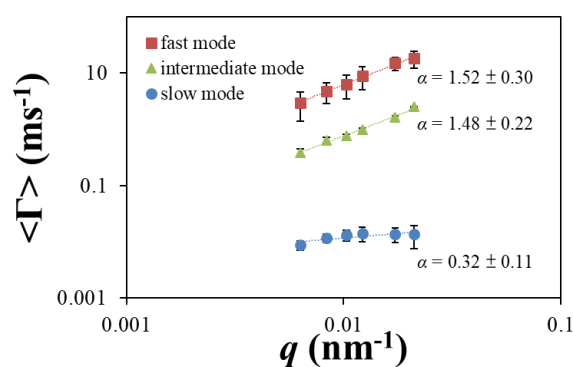


Fig. S10 Mean decay rate ($\langle \Gamma \rangle$) as a function of the scattering vector q , $\langle \Gamma \rangle \sim q^\alpha$, for the 10 mg mL⁻¹ Lw-pBTTT-C₁₆/CB sol ($T = 15$ °C, $t = 0$ h).

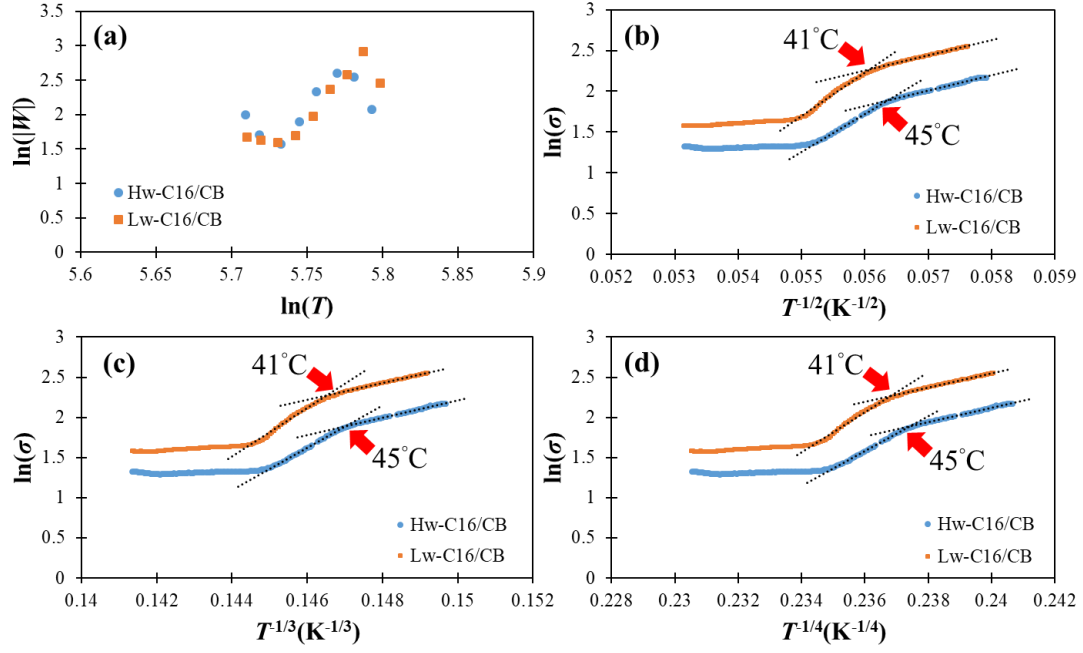


Fig. S11 Model fits using the variable range hopping (VRH) model,^{7,8} $\sigma = \sigma_0 \exp[-(T_0/T)^\gamma]$, where σ is the ac-conductivity at a particular temperature (T), σ_0 is the pre-exponential factor, T_0 is a characteristic temperature, and γ is a constant that depends on dimensionality of the process. In general, when plotting $\ln W$ versus $\ln T$, where $W = d \ln \sigma / d \ln T$, the slope yields γ and the implied dimensionality for the underlying hopping mechanism. Noticing, however, that the value of W is negative for the pBTTT-C₁₆/CB samples investigated herein, because σ increases with reduced system temperature as observed in Fig. 1 of the main text, the absolute value $|W|$ is used instead for the plots shown in (a). Clearly, the observed trends cannot be described by the usual electron-hopping mechanisms. Alternatively, (b)-(d) present the results based on the 1-D, 2-D, and 3-D versions of the VRH model, respectively, and the intersection points for each pBTTT-C₁₆/CB sample shown in these plots in the low-temperature region correspond approximately to the same temperature which is very close to the gelation temperature inferred previously from dynamic modulus/light scattering analyses (i.e., $T_{\text{Gel}} \sim 42$ and 48 °C for Lw-pBTTT-C₁₆/CB and Hw-pBTTT-C₁₆/CB, respectively.)

Table S2 Parameter values extracted from full-curve fits of DLS and DDLS data on the Lw-pBTTT-

C₁₆/CB sample at two representative gelation times at 15 °C

State	Parameters	Method	
		DLS	DDLS
gelation time, <i>t</i> = 0 h	Fraction of the fast mode (A)	0.003±0.006	0.12±0.02
	Length of isolated rodlike gelator (<i>L</i>) [nm]	15.8±0.2	15.9±0.2
	Diameter of isolated rodlike gelator (<i>d</i>) [nm]	4.5±0.1	4.6±0.2
	Stretch exponent (α)	0.71±0.01	0.94±0.25
	Aspect ratio	3.5	3.4
	Fraction of the collective diffusion mode (B)	0.56±0.12	0.88±0.09
	Length of cylindrical aggregate (<i>L</i>) [nm]	155±2	231±2
	Diameter of cylindrical aggregate (<i>d</i>) [nm]	27±11	67±15
	Stretch exponent (β)	1.13±0.22	0.51±0.02
	Aspect ratio	5.8	3.4
Characteristic time (<i>t_c</i>) [ms]	79.7±4.3	502±36	
Stretch exponent (γ)	2.02±0.03	1.33±0.20	
gelation time, <i>t</i> = 16 h	Fraction of the fast mode (A)	0.001±0.001	-
	Length of isolated rodlike gelator (<i>L</i>) [nm]	15.4±0.4	-
	Diameter of isolated rodlike gelator (<i>d</i>) [nm]	4.4±0.3	-
	Stretch exponent (α)	0.14±0.18	-
	Aspect ratio	3.5	-
	Fraction of the collective diffusion mode (B)	0.30±0.05	-
	Length of cylindrical aggregate (<i>L</i>) [nm]	133±4	-
	Diameter of cylindrical aggregate (<i>d</i>) [nm]	42±1	-
	Stretch exponent (β)	0.57±0.04	-
	Aspect ratio	3.2	-
Characteristic time (<i>t</i> [*]) [ms]	16.7±2.8	-	
Power-law exponent (<i>n</i>)	0.24±0.17	-	

S5 Expressions for model fits of SALS/SLS/SAXS data

$$I_{\text{SALS+SLS}}(q) = I_G(0)\exp\left(-\frac{1}{3}R_g^2q^2\right) + \frac{I_L(0)}{\{1+[(d_f+1)/3]\zeta^2q^2\}^{d_f/2}}P_{\text{cyl, agg}}(q) \quad (\text{S1})$$

$$P_{\text{cyl}}(q) = \int_0^{\pi/2} \left(\frac{\sin\left(\frac{qL}{2}\cos\varphi\right) 2J_1(qR\sin\varphi)}{\left(\frac{qL}{2}\cos\varphi\right) (qR\sin\varphi)} \right)^2 \sin\varphi \, d\varphi \quad (\text{S2})$$

(Form factor for randomly oriented cylinders, with radius R and length L)

$$I_{\text{SAXS}}(q) = \frac{I_D(0)}{[1+q\zeta_d\exp(q^2R^2/4)]} + I_P(0)P_{\text{cyl, gelator}}(q) \quad (\text{S3})$$

Table S3 Gelation-time dependences of the crossover point in the SAXS profile that defines the mesh structure formed by cylindrical aggregate bundles for the Lw-pBTTT-C₁₆/CB Gel incubated at 15 °C

Parameters	Gelation time (h)				
	3	5	7	9	11
q_c [nm ⁻¹]	0.14	0.12	0.11	0.063	0.061
ξ [nm] ^a	44.9	52.4	57.1	99.7	103.0

^a Calculated from the relation $\xi = 2\pi / q_c$.

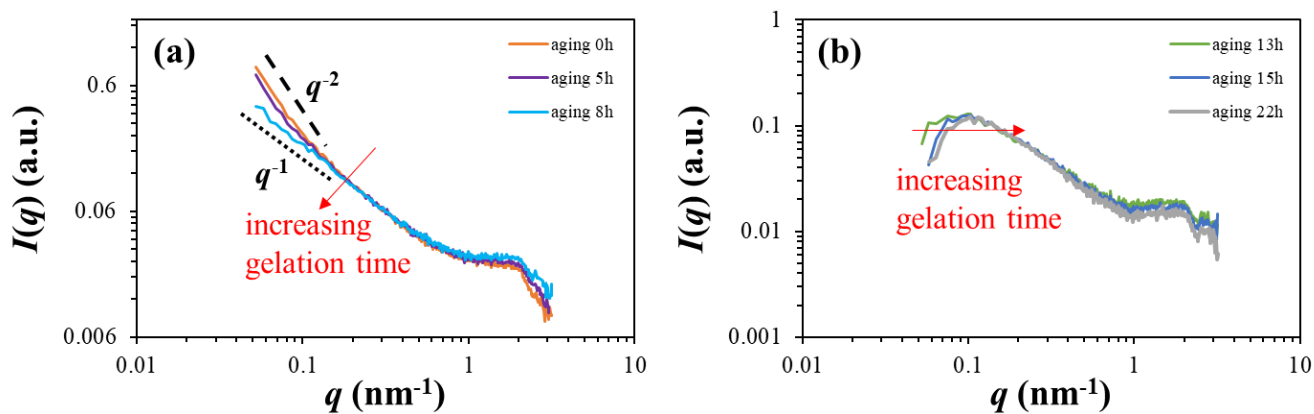


Fig. S12 Time evolutions of the SAXS profile for the Lw-pBTTT-C₁₆/CB gel incubated at 15 °C.

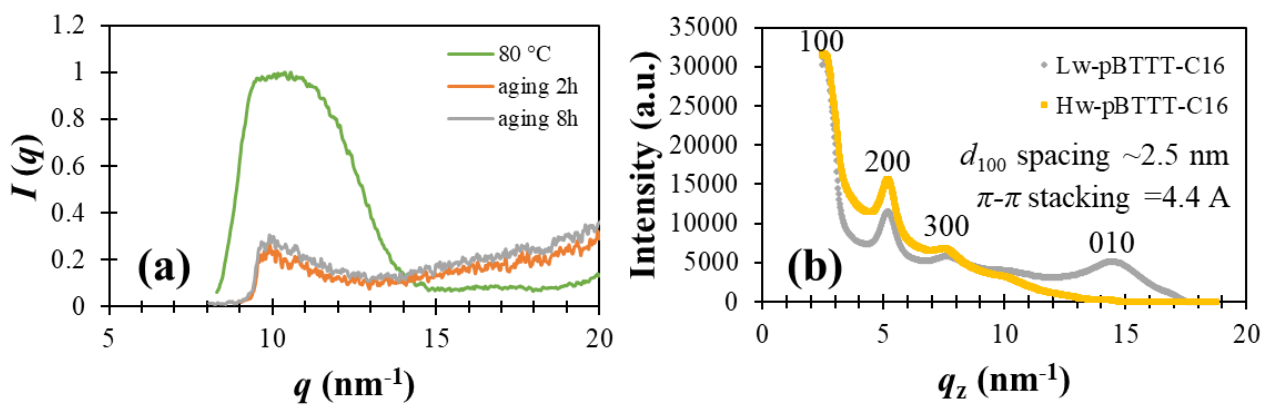


Fig. S13 (a) WAXS patterns for the Lw-pBTTT-C₁₆/CB solution and sol-gel at $T = 15$ °C; (b) GIWAXS patterns of the drop-cast thin films produced from the Hw-pBTTT-C₁₆/CB and Lw-pBTTT-C₁₆/CB solutions at room temperature.

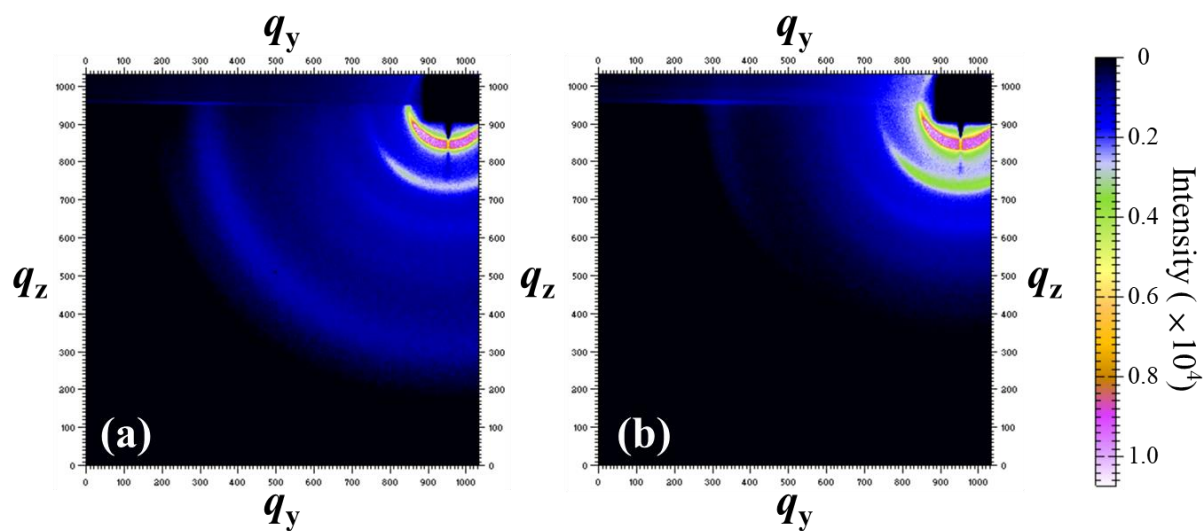


Fig. S14 GIWAXS images of the drop-cast thin films produced from the solutions of (a) Lw-pBTTT-C₁₆/CB and (b) Hw-pBTTT-C₁₆/CB at room temperature, where the profile along the q_z axis is plotted in Fig. S11b.

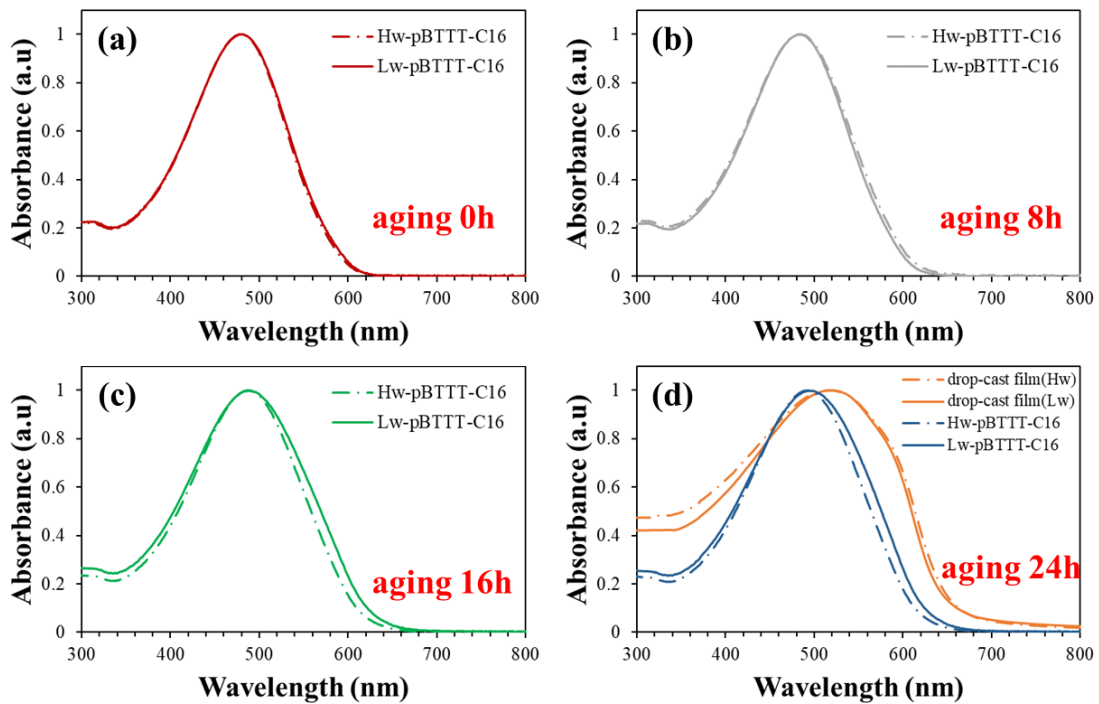


Fig. S15 Comparison of the time-evolving UV-vis absorption spectra during the gelation process at 15 °C between Lw-pBTTT-C₁₆/CB (solid lines) and Hw-pBTTT-C₁₆/CB (dash-dotted lines). For comparison, the results for drop-cast thin film (orange lines) are also shown in (d).

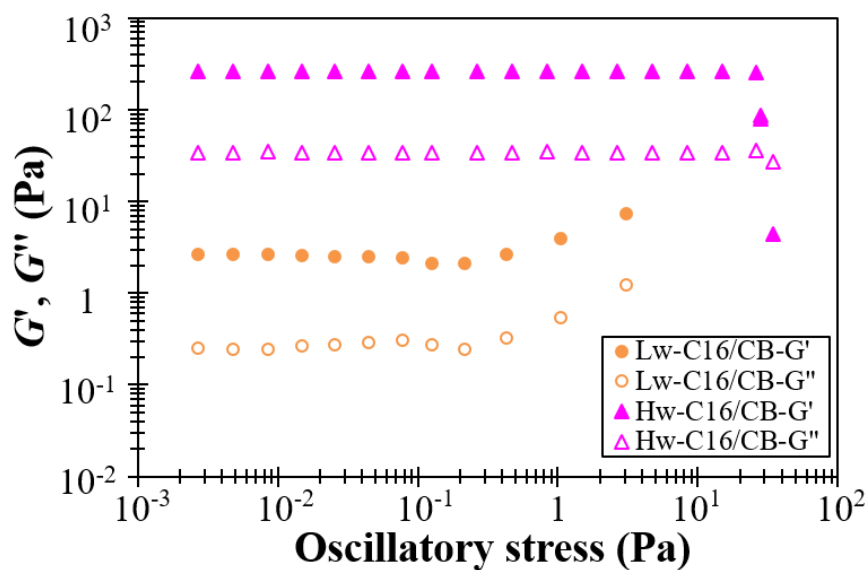


Fig. S16 Dynamic modulus responses as a function of oscillatory stress during strain sweep at a constant frequency of 10 rad/s for the gel incubated for 24 h at $T = 15$ °C. The break point in each case is identified as the maximal stress shown in this figure that precedes a notable stress reversal (not shown here).

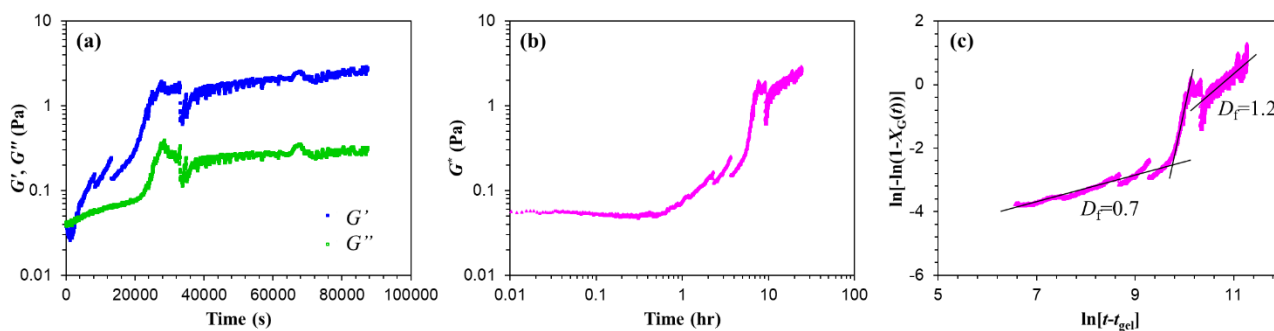


Fig. S17 Time-dependences of (a) the two dynamic moduli and (b) their magnitude (G^*) for the Lw-pBTTT-C₁₆/CB as a function of gelation time at 15 °C. (c) The Avrami plot using the results from (b).

References

1. H.-L. Yi and C.-C. Hua, *Soft Matter*, 2018, **14**, 1270-1280.
2. M. Takeda, T. Norisuye and M. Shibayama, *Macromolecules*, 2000, **33**, 2909-2915.
3. S. L. Elliott, R. J. Butera, L. H. Hanus and N. J. Wagner, *Faraday Discuss.*, 2003, **123**, 369-383.
4. F. Mallamace, P. Gambadauro, N. Micali, P. Tartaglia, C. Liao and S. H. Chen, *Phys. Rev. Lett.*, 2000, **84**, 5431-5434.
5. M. J. Solomon and P. Varadan, *Phys. Rev. E*, 2001, **63**, 051402.
6. H. L. Yi, C. H. Wu, C. I. Wang and C. C. Hua, *Macromolecules*, 2017, **50**, 5498-5509.
7. N. F. Mott, *J. Non-Cryst. Solids*, 1968, **1**, 1-17.
8. N. Mott, *Metal-Insulator Transitions*, Taylor & Francis, London, 1990.